

A Cost Effective and High Fidelity Fluoroscopy Simulator using the Image-Guided Surgery Toolkit (IGSTK)

Ren Hui Gong^c, Brad Jenkins^b, Raymond W. Sze^{a,b} and Ziv Yaniv^a

^aThe Sheikh Zayed Institute for Pediatric Surgical Innovation, Children's National Medical Center, Washington, DC 20010, USA

^bDepartment of Radiology, Children's National Medical Center, Washington, DC 20010, USA

^cDepartment of Radiation Oncology, School of Medicine, Stanford University, CA 94305, USA

ABSTRACT

The skills required for obtaining informative x-ray fluoroscopy images are currently acquired while trainees provide clinical care. As a consequence, trainees and patients are exposed to higher doses of radiation. Use of simulation has the potential to reduce this radiation exposure by enabling trainees to improve their skills in a safe environment prior to treating patients. We describe a low cost, high fidelity, fluoroscopy simulation system. Our system enables operators to practice their skills using the clinical device and simulated x-rays of a virtual patient. The patient is represented using a set of temporal Computed Tomography (CT) images, corresponding to the underlying dynamic processes. Simulated x-ray images, digitally reconstructed radiographs (DRRs), are generated from the CTs using ray-casting with customizable machine specific imaging parameters. To establish the spatial relationship between the CT and the fluoroscopy device, the CT is virtually attached to a patient phantom and a web camera is used to track the phantom's pose. The camera is mounted on the fluoroscope's intensifier and the relationship between it and the x-ray source is obtained via calibration. To control image acquisition the operator moves the fluoroscope as in normal operation mode. Control of zoom, collimation and image save is done using a keypad mounted alongside the device's control panel. Implementation is based on the Image-Guided Surgery Toolkit (IGSTK), and the use of the graphics processing unit (GPU) for accelerated image generation. Our system was evaluated by 11 clinicians and was found to be sufficiently realistic for training purposes.

Keywords: simulation, x-ray fluoroscopy, digitally reconstructed radiograph (DRR), graphics processing unit (GPU), tracking, image-guided surgery toolkit (IGSTK)

1. INTRODUCTION

Currently, medical training is still primarily based on the apprenticeship model, often referred to as "see one, do one, teach one". That is, the trainees observe procedures performed by experts and then acquire and improve their skills by providing patient care. This approach exposes both patients and clinicians to potential harm associated with the training process, conflicting with the ethical principle of nonmaleficence (first, do no harm). Simulation based training has been identified as a promising approach towards reducing the amount of harm associated with medical training in multiple clinical disciplines.¹⁻³ This approach enables the trainees to acquire and improve their skills prior to providing clinical care.

Simulation has made inroads into both diagnostic and interventional radiology.^{4,5} Both of these clinical specialties utilize imaging modalities, CT and x-ray fluoroscopy, that expose patients to ionizing radiation. Exposure to ionizing radiation has long been a concern in the general patient population. This is even more of a concern in the pediatric population, with clinicians encouraged to make judicious use of x-ray and CT imaging.^{6,7} In procedures utilizing intraoperative x-ray imaging, simulation has been shown to be an effective tool for improving the trainee's understanding of the principles of image acquisition and radiation exposure,⁸ and in reducing radiation exposure while improving performance in clinical care.⁹

E-mail: rhgong@stanford.edu; {brjenkin,rsze,zyaniv}@childrensnational.org.



Figure 1. Simulator setup in the clinical environment and its key components: (a) physical phantom component of the patient model; (b) web camera tracking the pose of the patient phantom; (c) keypad controlling simulated imaging functionality; (d) workstation providing computation and visualization. Arrows indicate the degrees of freedom in positioning the intensifier and the virtual patient. The image-intensifier has three, translational, degrees of freedom and the patient bed has one, rotational, degree of freedom.

We have developed a simulator for training clinicians to perform x-ray fluoroscopy based diagnosis. Our target procedure is the voiding cystourethrography (VCUG) examination. The VCUG examination is a method for studying the bladder and urethra using x-ray fluoroscopy while the patient is voiding (urinating). It is commonly performed in children that experience recurring urinary tract infections, have voiding abnormalities, or have been prenatally diagnosed with hydronephrosis.¹⁰ This is the most common fluoroscopy based imaging procedure in pediatric radiology departments,¹¹ with more than 900 cases performed in 2012 at our hospital, Children's National Medical Center. Recent studies have shown that the amount of radiation associated with this procedure is not negligible,¹² and that trainees expose patients to higher radiation doses than experienced radiologists.¹³

Simulation systems can be classified based on their fidelity,¹⁴ from low fidelity textual based simulators to high fidelity simulators that enable patient specific simulation with tactile feedback (e.g. Angio Mentor from Symbionix Ltd, Lod, Israel). In most cases cost and fidelity are correlated. In this work we describe a low cost, yet high fidelity fluoroscopy simulator.

Our goal is to train the clinicians in operating the x-ray machine, using a virtual patient and simulated x-ray imaging. That is, they should become proficient in positioning it relative to the patient to acquire the desired image with the relevant collimation and zoom. To increase the fidelity of our system we use spatio-temporal data, a set of CT images that represent the patient over time. This allows the trainees to practice timed image acquisition, a skill required for performing the VCUG procedure, documenting the progress of a contrast agent during voiding. In addition, we mimic the controls available on the specific fluoroscopy machine in use at our institution which include: collimation, zoom, inversion of intensities, saving a specific image, and an alarm indicating that 5min of fluoroscopy time have elapsed. To keep the cost of our system to a minimum we use web camera based tracking to estimate the relationship between the virtual patient and the imaging device, and a standard USB keypad to control all other functions. The detailed description of our system is given in the

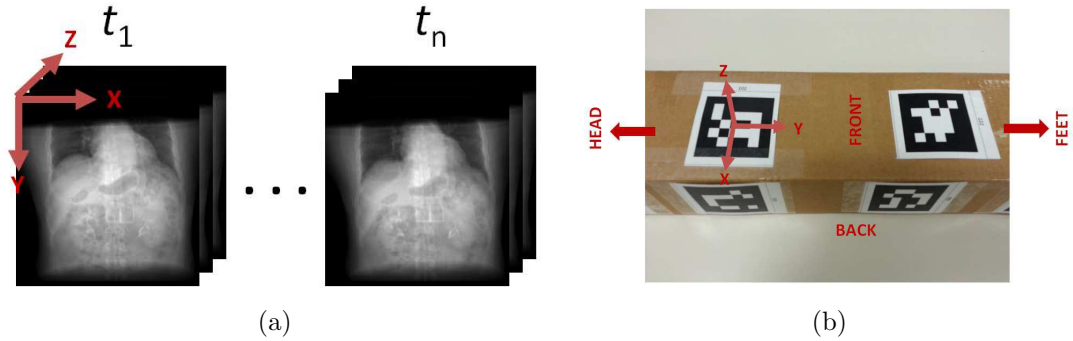


Figure 2. The patient model is comprised of a virtual patient (a): a specific sequence of temporal CT images; and a generic physical phantom (b): box with attached markers, enabling tracking through a wide range of poses. The virtual patient is transformed to the physical phantom using the mapping overlaid in (b). Note that this is an arbitrary, user defined, transformation.

following section.

2. METHODS

The key elements of our simulator include: (1) a patient model, consisting of a virtual patient and a physical phantom; (2) web camera based tracking of the physical phantom; (3) methods for estimating the machine specific settings; (4) methods for generating DRRs, simulated x-ray images; and (5) operation and control of the simulator. Figure 1 shows our simulator in the clinical setting.

2.1 Patient Model

The patient model consists of an image based virtual patient and a physical phantom which are shown in Figure 2.

The image based virtual patient is a 4D (3D+time) CT. This enables simulation of dynamic processes such as breathing or movement of contrast. Our system allows the user to specify the set of CT volumes, and associate a time-stamp with each of the volumes. The time-stamp indicates that this volume represents the patient starting at the given time, from the beginning of the simulation. Note that this approach accommodates a 3D patient representation without any modifications, as the user need only provide a single CT volume, setting its time stamp to zero.

The physical phantom is a box with multiple markers attached to it, allowing the web camera to track it across a wide range of poses, including rotation around its long axis of $\pm 90^\circ$ which was a requirement for the VCUG procedure. This form of generic phantom is not appropriate for all simulations, specifically simulations in which the clinician needs to directly interact with the patient (e.g. bending the knee). In that setting a mannequin would be more appropriate. In the case of imaging for VCUG the clinicians do not directly interact with the patient. To acquire informative images they either move the image intensifier or rotate the patient's bed. Their focus is on the screen while they perform these changes, making our phantom appropriate for this setting.

Finally, the user needs to provide the transformation between the CT coordinate system and one of the tracked markers. We refer to this as the *root* marker. This is an arbitrary transformation, as it depends on the contents of the specific CT and on the choice of the *root* marker. In addition, the selection should be somewhat consistent with the physical world. That is, the CT's head to foot direction is expected to be aligned with the long axis of the box, and the offset between the physical phantom and the CT should be minimal. This ensures that the virtual patient is indeed close to the physical location of our generic phantom. Figure 2(b) visually illustrates this. An implicit assumption of our system is that all CTs share the same coordinate system which is always true for a clinical 4D CT.

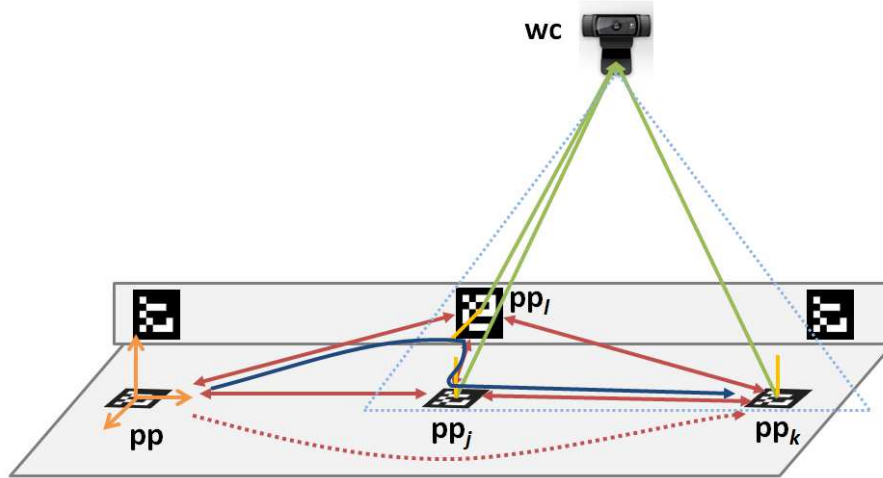


Figure 3. Calibration and tracking of a composite marker: When performing calibration the transformation between marker k and the *root* was estimated using the shortest path algorithm which identified the path as going from k to j , then to l and finally to the *root*. During tracking, when multiple markers are visible, the marker with the minimal ray-to-normal angle is selected, marker k in this illustration. The ray we use is the one originating at the camera and going through the markers center, the origin of its coordinate system.

2.2 Web Camera Based Tracking

To track the pose of our phantom using a calibrated web camera we utilize printed planar markers. Tracking a single marker is performed using the ArucoTracker component of the IGSTK.^{15,16} The web camera we use is the Logitech HD Pro C920. In our setting, using a single marker to track the phantom in all relevant poses is not possible. This is due to the limited field of view of the camera and the need to rotate the patient with an angle of 90° , relative to the camera.

We solve this limitation by using a composite marker. In our case, we define a *root* marker, relative to which the user specified the location of the virtual patient, and a set of markers with known rigid relationships to the *root*. Ideally, the transformations between the set of markers would be known by accurate construction. This is a restrictive approach and can potentially increase the cost of the phantom. As we aim to be cost effective and user friendly, we opt for a different solution. We allow the user to position the markers in arbitrary locations and then perform calibration, estimating the transformations. We next describe in detail our calibration process and our approach to tracking the composite marker.

2.2.1 Composite Marker Calibration

The goal of the calibration process is to estimate the transformations between the *root* marker and all other markers (e.g. T_{pp}^{ppk} in Figure 3).

Calibration is performed by repeatedly changing the pose of the phantom in front of the camera, and updating the dual transformations between each pair of visible markers. In the example shown in Figure 3, markers l , j and k are visible to the camera, and T_{ppl}^{ppj} (T_{ppj}^{ppi}), T_{ppi}^{ppk} (T_{ppk}^{ppi}), and T_{ppj}^{ppk} (T_{ppk}^{ppj}) will be updated. The transformations between two neighboring markers are computed using the tracked poses of the end markers as

$$T_a^b = (T_b^{wc})^{-1}T_a^{wc}, \quad T_b^a = (T_a^{wc})^{-1}T_b^{wc} \quad (1)$$

where a and b are the two neighboring markers, and wc is the web camera. Each edge connecting two neighboring markers is associated with a quality measure, and the transformations associated with the edge are updated only if the edge quality is improved. The edge quality is defined using the pose qualities of the two end markers. The pose quality of a marker is measured using the transformation from the marker to the camera. We chose to use the angle between the ray originating at the camera and going through the center of the marker, and the

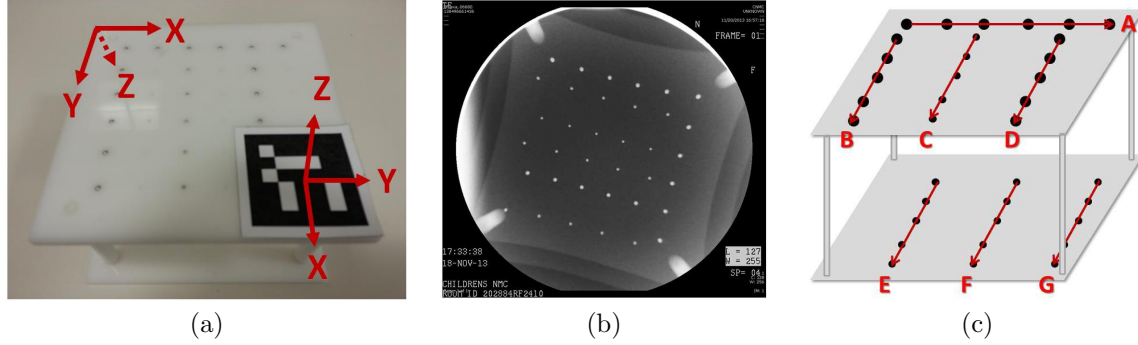


Figure 4. X-ray calibration: (a) 3D phantom; (b) x-ray image; and (c) grid structure used to establish point correspondences between the 3D model and image points.

marker's normal direction to measure the quality of the marker's pose, the smaller is the angle, the higher is the pose quality. Using a conservative approach, we set the edge quality to be the smaller pose quality of the two estimates.

This process continues until we have a connected graph which assures that there is a path from every node to the root. In this graph the vertices represent the markers and the edges represent the transformations between them. Upon termination, every marker has one or more paths to the *root* marker. Using Dijkstra's shortest path algorithm¹⁷ we compute the transformation between every marker and the *root*, by composing the transformations along the shortest path. In the example shown in Figure 3, T_{pp}^{ppk} is estimated as a composition of transformations along the path from marker k , to j , to l , and finally to the *root* marker.

Note that this calibration process requires that each of the markers is visible at least once, and at least one of its neighboring markers is visible at the same time. Testing for graph connectivity, our termination criterion, is done in the background, while the user manipulates the phantom.

2.2.2 Composite Marker Tracking

The pose of the *root* marker with respect to the web camera can be estimated as long as at least one marker, k , is visible in the image. This transformation is given by:

$$T_{pp}^{wc} = T_{ppk}^{wc} T_{pp}^{ppk}, \quad (2)$$

where pp and pp_k represent the root and k -th marker on the phantom respectively. T_{ppk}^{wc} is given by the tracking system, and T_{pp}^{ppk} is known from calibration (section 2.2.1).

There are cases when multiple markers are simultaneously visible to the camera. To select the specific marker we use the same quality measure as we did in the calibration process. That is, we select the marker which has the minimal angle between the ray originating at the camera and going through its center and its estimated normal in the camera coordinate system.

2.3 Estimation of Machine Specific Settings

To customize our simulator to a specific x-ray fluoroscopy machine we need to estimate its internal parameters so that we generate similar images. In addition we need to estimate the transformation relating our web camera to the x-ray device's coordinate system.

2.3.1 Estimation of Fluoroscopy Imaging Parameters

We model the x-ray fluoroscopy system using the standard pin-hole camera model. The model's imaging parameters include intrinsic parameters: focal length, location of the principal point in the x-ray image, and distortion coefficients, and extrinsic parameters: rigid transformation between the 3D model and the x-ray coordinate system. To estimate the machine specific parameter values we use a two plane calibration phantom embedded with 36 metal spheres, arranged in a regular grid. Figure 4 shows a picture of the calibration phantom and a sample

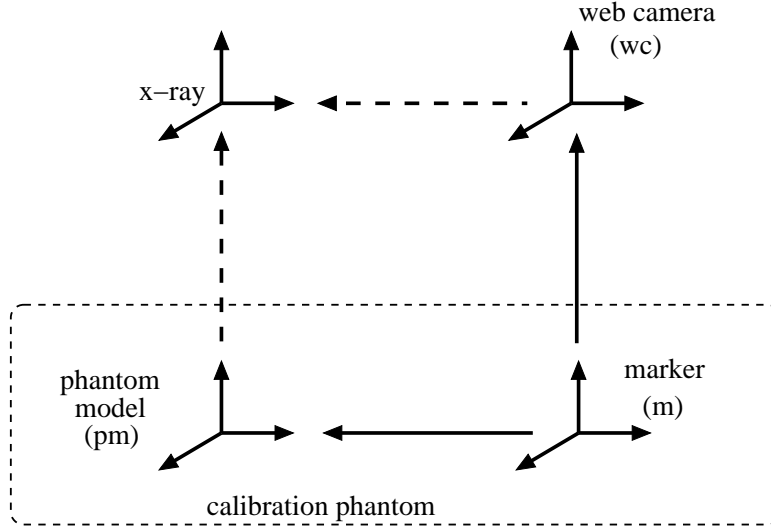


Figure 5. Transformations relating web camera to x-ray coordinate system. Solid (dashed) arrows denote known (unknown) transformations.

x-ray image. The sphere configuration defines seven line segments, Figure 4(c), which are used to establish the point correspondences between the phantom model and the points detected in the x-ray image.

Using the phantom, we estimate the imaging parameter values as follows:

1. Pre-process the x-ray image to detect the circular imaging field of view of the fluoroscopy device, and removing all textual information outside of the circle (reduces outliers in the subsequent detection steps).
2. Detect all points, and their diameters, via blob detection in the x-ray image.¹⁸
3. Establish point correspondences between the 3D phantom model and 2D x-ray points:
 - (a) Classify points into two groups based on diameter, using k-means (k=2) classification.
 - (b) Three lines (A, B, D in Figure 4(c)) are identified using the large points detected in the previous step using the RANSAC algorithm.¹⁹ Using the known configuration of the three lines, each of the image points is paired with its corresponding model point. Subsequently, the line formed by small points in the top layer is also detected, and each of the points on the line is identified.
 - (c) Using line B from the top layer as a reference, the lines on the bottom layer are detected from the remaining points, and each of the points on the lines is paired with its corresponding model point.
4. Using the correspondences established in the previous step, estimate the camera parameters using the LevenbergMarquardt algorithm via non-linear least squares.²⁰

2.3.2 Estimation of Web Camera to x-ray Transformation

The transformation between the web camera to the x-ray coordinate system is also estimated using the x-ray calibration phantom, as part of the calibration process. A marker which is tracked by the web camera is attached to the the calibration phantom, as shown in Figure 4(a). When the x-ray image is acquired the phantom's pose with respect to the web camera is also recorded.

We thus obtain the transformation from the web camera to the x-ray coordinate system as:

$$T_{wc}^{x-ray} = T_{pm}^{x-ray} T_m^{pm} (T_m^{wc})^{-1} \quad (3)$$

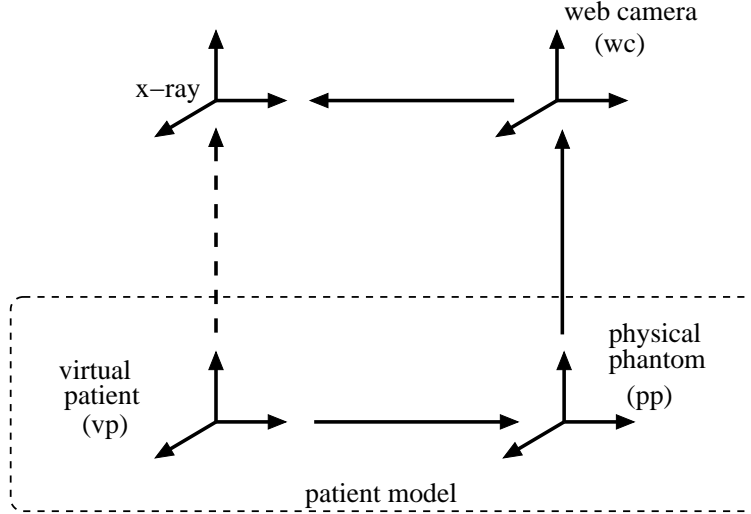


Figure 6. Computation of the patient model to intensifier transformation can be done by following the link through patient phantom and web camera.

where T_m^{pm} is known from construction, T_m^{wc} is the transformation reported by the web camera, and T_{pm}^{x-ray} corresponds to the extrinsic parameter values estimated using the 3D point coordinates in the phantom-model coordinate system. Figure. 5 shows the coordinate systems involved in this process. Note that it is also possible to compute T_{wc}^{x-ray} directly if instead of providing the 3D points in the phantom-model coordinate system we provide their coordinates in the web camera's coordinate system during the calibration process.

2.4 DRR Generation

We generate DRRs using a sampling based ray-casting approach. For a realistic simulation, we need to generate DRRs at real time or near real time speeds. We thus perform the computations on the Graphics Processing Unit (GPU). Using an NVIDIA GeForce GTX 560 Ti card, DRRs with a resolution of 512x512 were generated at an average rate of 11 frames per second. All computations were performed using floating point calculations.

As we are dealing with a 4D CT, our implementation uses two independent concurrent threads. The first thread queries the physical phantom's pose and generates DRRs from the active volume. The second thread monitors the time and loads the relevant volume based on the user provided time stamps. Prior to using the volume for DRR generation we map the Hounsfield units to attenuation coefficient values.

To simulate an x-ray image from the virtual patient, we need to know the transformation relating the virtual patient to the x-ray coordinate system. This transformation is obtained as:

$$T_{vp}^{x-ray} = T_{wc}^{x-ray} T_{pp}^{wc} T_{vp}^{pp}, \quad (4)$$

where T_{vp}^{pp} is the user specified transformation between the CT (virtual patient) coordinate system and the physical phantom coordinate system, T_{pp}^{wc} is the current pose of the *root* marker relative to the web camera, and T_{wc}^{x-ray} is the transformation between the web camera to the x-ray system estimated during the calibration process. Figure. 6 shows the coordinate systems involved in this process.

2.5 Simulator Operation and Control

In a typical fluoroscopy based procedure, the operator activates x-ray imaging and interactively positions the imaging device relative to the patient to acquire informative images. This is achieved by translating the image intensifier and in the case of VCUG, also rotating the patient. In addition the operator will often magnify regions of interest and use collimation to reduce radiation exposure. Other key functionalities include image

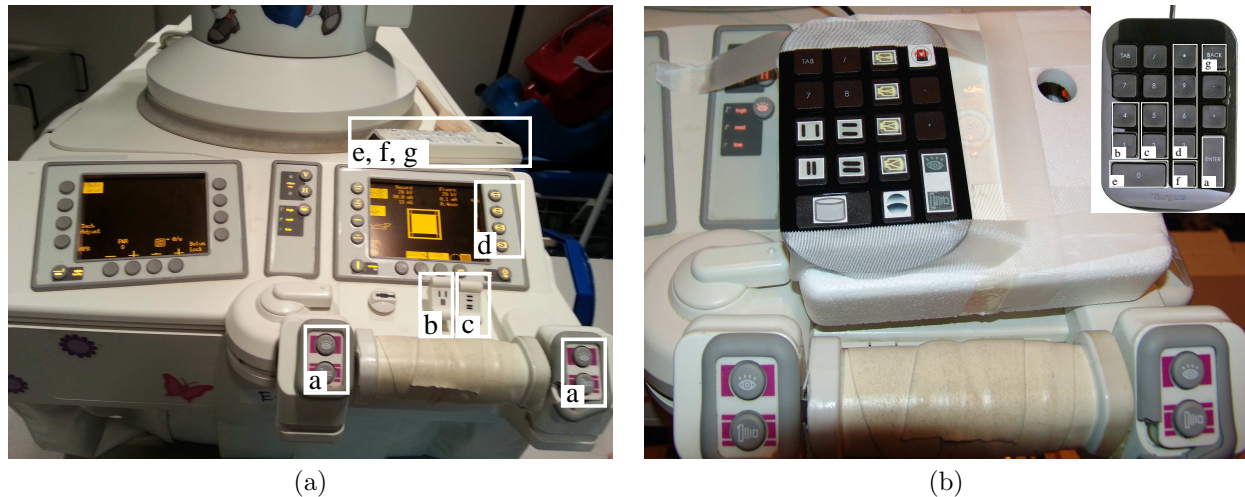


Figure 7. (a) Clinical control panel and (b) simulator control keypad mounted on top of the clinical one. Inset shows the corresponding functionalities, which include: a - activate fluoroscopy; b - horizontal collimation; c - vertical collimation; d - four magnification levels; e - save image to disk; f - invert intensities; g - reset dose alarm.

saving, inversion of the grayscale intensities to improve operator sensitivity, a fluoroscopy alarm which indicates that 5 minutes of fluoroscopy time have elapsed, and a reset button for this alarm.

Our goal designing the fluoroscopy simulator was to provide a user experience that is as similar as possible to that provided by the clinical machine. We use the actual clinical device to drive our simulation. Thus, the physical manipulation of the image intensifier and the patient bed remain the same as in the clinical setting. Ideally, one would only need to turn a switch and instead of controlling the x-ray machine functions the same buttons would control the simulator. This would ensure that skills obtained from using the simulator are directly transferable to the clinical setting. This is currently not possible. We therefore introduce a standard keypad which allows the operator to control all of these functions. The keypad is mounted over the clinical machine's controls, close to their actual locations. Figure 7 shows the mapping between the clinical machine controls and our keypad.

3. EXPERIMENTAL RESULTS

We conducted a survey based evaluation study of our simulator, assessing whether the accuracy with which it mimics the clinical system is sufficient. For this evaluation, we used a clinical 4D thoracic-abdominal scan as our virtual patient. This data set consists of ten CT volumes obtained throughout the respiratory cycle. Image size was $512 \times 512 \times 136$, with a voxel size of $0.98 \times 0.98 \times 2.5\text{mm}$.

Eleven clinicians with varying degrees of experience (6 attending, 3 fellows, 2 residents) participated in the study. None of the participants had prior experience with our simulator, but all of them were familiar with the functionality of the clinical system. All participants were given a 5 minute instructional session demonstrating the usage of the simulator before they evaluated the system. Each participant was then asked to use all functions of the simulator after which they answered the survey.

The survey included 11 statements using a five point Likert scale, from 1, strongly disagree, to 5, strongly agree. In addition, each participant also had the option to provide free form comments with regard to issues they identified with our simulator. Table 1 summarizes the results.

Overall our simulator was well received with an average score of 4.0 ± 0.9 . Note that the last statement in our questionnaire is phrased in the reverse. This is intentional, to allow us to identify respondents who are not paying attention to the specific statements, but repeatedly responding based on their overall impression of the system. Only one respondent, who was very positive about the system, indicated that he "strongly agreed" with this statement, contrasting with his responses to all other statements. The free form comments further

Question	Score (<i>score ± st.dev.</i>)
1 Collimation is realistic	3.8 ± 1.3
2 4-level zooming is realistic	3.8 ± 1.0
3 Fluoroscopic images are realistic	4.4 ± 0.5
4 Imaging responsiveness is realistic	4.1 ± 0.8
5 Dose alarm is realistic	4.2 ± 1.0
6 Image save is realistic	4.1 ± 1.1
7 Control pad closely mimics the clinical hardware	3.5 ± 1.2
8 4D CT to model a dynamic physiologic process is realistic	4.1 ± 0.6
9 Use of a patient phantom is sufficiently realistic	4.0 ± 0.8
10 The range of motion the system provides is realistic (positioning of virtual patient and motion of imager)	4.5 ± 0.5
11 Hardware setup, wire connections, computer placement detracts from the system's realism	4.1 ± 0.8
Overall	4.0 ± 0.9

Table 1. Summary of questionnaire answers (Score: 1 - Strongly Disagree; 2 - Disagree; 3 - No Opinion; 4 - Agree; 5 - Strongly Agree).

elaborated on the issues some users had with our system. These corresponded to the statements which received the lower scores.

The main issues operators had with our system include:

- *Collimation.* Our simulator updates the collimated image without the need for active fluoroscopy. This differs from the behavior of the fluoroscopy unit we have at our institution. For our clinical device, change in collimation is only visible once the operator acquires a new image. That is, fluoroscopy must be activated. After further discussion with our clinical collaborators, it turns out that the newer generation of fluoroscopy machines do reflect changes in collimation without the need for active imaging. This is referred to as electronic or virtual collimation.
- *Zooming.* At higher magnification levels our images exhibit pixelation. This issue is due to the limited computation capability of the mid-range consumer GPU used in our experiments. We will address this issue by switching to a higher-end GPU. This will allow us to improve the rendering quality while maintaining the frame rate.
- *Control pad.* The difference between our keypad and the clinical control pad is significant and was noted by most operators. To improve the user experience we would have to design a custom control panel similar to that of our machine, which would increase the cost of our simulator. While this would allow the clinicians to acquire the motor skills associated with acquiring images using a specific machine, it does not generalize well. The functionality of these machines is similar, but the controls are vendor specific. We therefore will continue to use the keypad as our control mechanism.

4. DISCUSSION AND CONCLUSIONS

Simulation based training has made significant inroads into the radiology training curriculum.^{4,5} Unfortunately, high fidelity simulation is most often costly. As a consequence it is only available at institutions which have the financial resources to maintain high end simulation centers. In this paper we presented a cost effective, high fidelity x-ray fluoroscopy simulator. This approach has the potential for widespread adoption due to its inherent low cost while providing a user experience which is similar to the clinical one.

Simulation of x-ray imaging was previously proposed by several research groups. In cardiology, a software based simulation system was described in.²¹ This system modeled the patient as a set of polygonal objects corresponding to anatomical structures. Hemodynamic fluid flow computations were used to simulate anatomical motion. x-ray image acquisition was performed via a software interface, allowing the operator to control a virtual

C-arm. A similar approach to controlling x-ray simulation is used in several commercial systems such as the ANGIO Mentor and URO Mentor from Symbionix Ltd. (Lod, Israel).

In orthopedics, a system using a combination of software and a 1/6 scaled model of a C-arm and patient was described by Jaramaz and Eckman.²² This system allowed the operator to control image acquisition by manually positioning a miniature C-arm relative to a mock patient. Both the C-arm and patient were tracked using a commercial optical tracking system. The patient anatomy is assumed to be stationary. Another system, in the context of orthopedics, was described by Dressel et al.²³ That system used monocular optical tracking to track printed markers and assumed a stationary patient. The x-ray imaging device used in that work is unique as it combines a video camera as part of the C-arm structure, providing augmented reality views for orthopedic procedures by fusing video and x-ray.

The most similar work to our own is that described by Bott et al.⁸ In that setting a mannequin is used to simulate the patient and a standard C-arm is used to control image acquisition. Both mannequin and C-arm are tracked using a commercial electromagnetic tracking system. The patient can be moved as tracking sensors are attached to the relevant body parts (e.g. hip, thigh), although these do not simulate dynamic processes such as respiration.

Our simulator is based on the use of a clinical fluoroscopy device and customized to its specific imaging parameters. We use a simple patient phantom which is appropriate for simulating image acquisition, where the focus is on the screen and not on the patient. The virtual patient associated with our physical phantom represents dynamic processes allowing us to generate x-ray images exhibiting respiratory motion. To reduce the costs associated with our system we use a web camera and printed markers to perform tracking, and a keypad to control all simulator functionality. Based on our evaluation study we conclude that our system is sufficiently realistic for medical training, and has the potential to increase trainees imaging skills in a safe environment before they begin providing clinical care.

REFERENCES

- [1] Ziv, A., Wolpe, P. R., Small, S. D., and Glick, S., "Simulation-based medical education: An ethical imperative," *Acad Med.* **78**(8), 783–788 (2003).
- [2] Rosen, K. R., "The history of medical simulation," *J Crit Care.* **23**(2), 157–166 (2008).
- [3] Rodriguez-Paz, J. M., Kennedy, M., Salas, E., Wu, A. W., Sexton, J. B., Hunt, E. A., and Pronovost, P. J., "Beyond "see one, do one, teach one": toward a different training paradigm," *Qual Saf Health Care* **18**(1), 63–68 (2009).
- [4] Gould, D., "Using simulation for interventional radiology training," *Br J Radiol.* **83**(991), 546–553 (2010).
- [5] Sabir, S. H., Aran, S., and Abujudeh, H., "Simulation-based training in radiology," *J Am Coll Radiol.* (in press).
- [6] Sidhu, M., Coley, B. D., Goske, M. J., Connolly, B., Racadio, J., Yoshizumi, T. T., Utley, T., and Strauss, K. J., "Image gently, step lightly: increasing radiation dose awareness in pediatric interventional radiology," *Pediatr Radiol.* **39**(10), 1135–1138 (2009).
- [7] Hernanz-Schulman, M., Goske, M. J., Bercha, I. H., and Strauss, K. J., "Pause and pulse: ten steps that help manage radiation dose during pediatric fluoroscopy," *AJR Am J Roentgenol* **197**(2), 475–481 (2011).
- [8] Bott, O. J., Dresing, K., Wagner, M., Raab, B.-W., and Teistler, M., "Use of a C-Arm fluoroscopy simulator to support training in intraoperative radiography," *Radiographics* **31**(3), E65–E75 (2011).
- [9] Ponti, R. D., Marazzi, R., Doni, L. A., et al., "Simulator training reduces radiation exposure and improves trainees performance in placing electrophysiologic catheters during patient-based procedures," *Heart Rhythm* **9**(8), 1280–1285 (2012).
- [10] Fernbach, S. K., Feinstein, K. A., and Schmidt, M. B., "Pediatric voiding cystourethrography: a pictorial guide," *Radiographics* **20**(1), 155–168 (2000).
- [11] Schneider, K., Stollfuß, I. K., Ernst, G., and Kohn, M. M., "Paediatric fluoroscopy—a survey of children's hospitals in europe. i. staffing, frequency of fluoroscopic procedures and investigation technique," *Pediatr Radiol.* **31**(4), 238–246 (2001).

- [12] Lee, R., Thomas, K. E., Connolly, B. L., Falkiner, M., and Gordon, C. L., “Effective dose estimation for pediatric voiding cystourethrography using an anthropomorphic phantom set and metal oxide semiconductor field-effect transistor (MOSFET) technology,” *Pediatr Radiol.* **39**(6), 608–615 (2009).
- [13] Lim, R., Khawaja, R. D. A., Nimkin, K., Sagar, P., Shailam, R., Gee, M. S., and Westra, S. J., “Relationship between radiologist training level and fluoroscopy time for voiding cystourethrography,” *AJR Am J Roentgenol.* **200**(3), 645–651 (2013).
- [14] Datta, R., Upadhyay, K. K., and Jaideep, C. N., “Simulation and its role in medical education,” *Medical Journal Armed Forces India* **68**(2), 167–172 (2012).
- [15] Enquobahrie, A., Gobbi, D., Turek, M. W., Cheng, P., Yaniv, Z., Lindseth, F., and Cleary, K., “Designing tracking software for image guided surgery applications: IGSTK experience,” *International Journal of Computer Assisted Radiology and Surgery* **3**(5), 395–403 (2008).
- [16] Özgür Güler and Yaniv, Z., “Image-guided navigation: A cost effective practical introduction using the image-guided surgery toolkit (IGSTK),” in [*International Conference of the IEEE Engineering in Medicine and Biology Society (EMBC)*], (2012).
- [17] Dijkstra, E. W., “A note on two problems in connexion with graphs,” *Numerische Mathematik* **1**, 269–271 (1959).
- [18] Lindeberg, T., “Feature detection with automatic scale selection,” *International Journal of Computer Vision* **30**(2), 79–116 (1998).
- [19] Fischler, M. A. and Bolles, R. C., “Random sample consensus: a paradigm for model fitting with applications to image analysis and automated cartography,” *Commun. ACM* **24**(6), 381–395 (1981).
- [20] Hartley, R. I. and Zisserman, A., [*Multiple View Geometry in Computer Vision*], Cambridge University Press (2000).
- [21] Dawson, S. L., Cotin, S., Meglan, D., Shaffer, D. W., and Ferrell, M. A., “Designing a computer-based simulator for interventional cardiology training,” *Catheter Cardiovasc Interv.* **51**(4), 522–527 (2000).
- [22] Jaramaz, B. and Eckman, K., “Virtual reality simulation of fluoroscopic navigation,” *Clin Orthop Relat Res* **442**, 30–34 (2006).
- [23] Dressel, P., Wang, L., Kutter, O., Traub, J., Heining, S.-M., and Navab, N., “Intraoperative positioning of mobile C-arms using artificial fluoroscopy,” in [*SPIE Medical Imaging: Visualization, Image-Guided Procedures, and Modeling*], 762506–762506–6 (2010).